nature
physics

Check for updates

Unperturbed inverse kinematics nucleon knockout measurements with a carbon beam

M. Patsyuk[1,2], J. Kahlbow[1,3], G. Laskaris[1,3], M. Duer[4], V. Lenivenko[2], E. P. Segarra[1], T. Atovullaev[2,5], G. Johansson[3], T. Aumann [4,6,7], A. Corsi[8], O. Hen [1 ✉], M. Kapishin[2], V. Panin[6,8], E. Piasetzky[3] and The BM@N Collaboration*

Particle knockout scattering experiments[1,2] are fundamental for mapping the structure of atomic nuclei[2-6], but their interpretation is often complicated by initial- and final-state interactions of the incoming and scattered particles[1,2,7-9]. Such interactions lead to reduction in the scattered particle flux and distort their kinematics. Here we overcome this limitation by measuring the quasi-free scattering of 48 GeV c^{-1} ^{12}C ions from hydrogen. The distribution of single protons is studied by detecting two protons at large angles in coincidence with an intact ^{11}B nucleus. The ^{11}B detection suppresses the otherwise large distortions of reconstructed single-proton distributions induced by initial- and final-state interactions. By further detecting residual ^{10}B and ^{10}Be nuclei, we also identified short-range correlated nucleon–nucleon pairs[9-13] and provide direct experimental evidence for separation of the pair wavefunction from that of the residual many-body nuclear system[9,14]. All measured reactions are well described by theoretical calculations that include no distortions from the initial- and final-state interactions. Our results showcase the ability to study the short-distance structure of short-lived radioactive nuclei at the forthcoming Facility for Antiproton and Ion Research (FAIR)[15] and Facility for Rare Isotope Beams (FRIB)[16] facilities, which is relevant for understanding the structure and properties of nuclei far from stability and the formation of visible matter in the Universe.

Strongly interacting systems are difficult to study. In the special case of strongly interacting quantum gases, ground-state properties can be directly measured using ultracold atomic traps, where one can instantaneously turn off both the interactions between the atoms and the trap itself[17]. This allows the exploration of a wide range of fundamental quantum mechanical phenomena and the imitation of strongly correlated states in condensed matter systems where similar control over interparticle interactions cannot be obtained[18].

Due to their high density and complex strong interaction, constructing such model systems for atomic nuclei is extremely challenging. Instead, the distribution of nucleons in the nuclei is traditionally studied using high-energy electron scattering experiments that detect the scattered electron and knockout nucleon with high-resolution spectrometers[2]. The initial-state interaction and final-state interaction (ISI/FSI) lead to multistep processes that—depending on their kinematics—lead to a reduction in the quasi-elastic (QE) cross-section (attenuation) or kinematical distortion of the reconstructed single-nucleon ground-state properties.

At high energies, Glauber approximation calculations allow to estimate the total contribution of multistep ISI/FSI processes, while the relative contributions of distortion and attenuation are challenging to model. The pre-selection of the reaction kinematics or post-selection of the residual nucleus can suppress ISI/FSI distortions, which allow the use of energy and momentum conservation to reconstruct the distribution of nucleons in the nucleus. For these cases, the remaining attenuation effects can be estimated using Glauber approximation calculations[2,9,13,19,20].

Although largely limited to stable nuclei, such experiments have helped establish the nuclear shell model[2] and the existence and dynamics of short-range correlated (SRC) nucleon pairs[6,10,12,19] that constitute the next substantial approximation to the nuclear structure after the shell model[2,9,13].

Extending these studies to radioactive nuclei far from nuclear stability is a growing frontier of nuclear science[7]. Such studies require performing scattering experiments in inverse kinematics, where low-luminosity high-energy beams of radioactive nuclei are scattered from protons in hydrogen targets[21]. The cross-section for such reactions is much higher than that for electron scattering, but it comes at the price of large ISI that prevents kinematical pre-selection. Additionally, since there is rarely sufficient energy resolution to determine the residual nuclear state from the measured momenta of the knocked-out nucleons, post-selection requires the direct detection of the residual nuclear system[22].

Here we use post-selection in high-energy inverse kinematics $(p, 2p)$ scattering to probe single-particle states and SRCs in the well-understood ^{12}C nucleus. By detecting a bound nuclear fragment, we select the transparent part of the scattering reaction, where the measured events are predominantly due to single-step scattering reactions. Thus, multiple scattering ISI/FSI events, which would normally induce both attenuation and distortion, only lead to enhanced attenuation allowing for unperturbed reconstruction of particle distributions.

By identifying the ^{11}B fragment, we successfully study the distribution of protons in the p shell of ^{12}C, where we obtain consistent distributions for both QE and inelastic (IE) scattering reactions. Selecting ^{10}B and ^{10}B fragments, we further identify the hard breakup of SRC pairs. We directly measure the pair motion in the nucleus and establish the separation of the strong interpair interaction from the residual nuclear system. The latter is a key feature of modern theoretical SRC models[9,11,13,14,23], which has not been experimentally confirmed.

[1]Massachusetts Institute of Technology, Cambridge, MA, USA. [2]Joint Institute for Nuclear Research, Dubna, Russia. [3]School of Physics and Astronomy, Tel Aviv University, Tel Aviv, Israel. [4]Institut für Kernphysik, Technische Universität Darmstadt, Darmstadt, Germany. [5]Dubna State University, Dubna, Russia. [6]GSI Helmholtzzentrum für Schwerionenforschung GmbH, Darmstadt, Germany. [7]Helmholtz Forschungsakademie Hessen für FAIR, Frankfurt, Germany. [8]IRFU, CEA, Université Paris-Saclay, Gif-sur-Yvette, France. *A list of authors and their affiliations appears at the end of the paper. ✉e-mail: hen@mit.edu
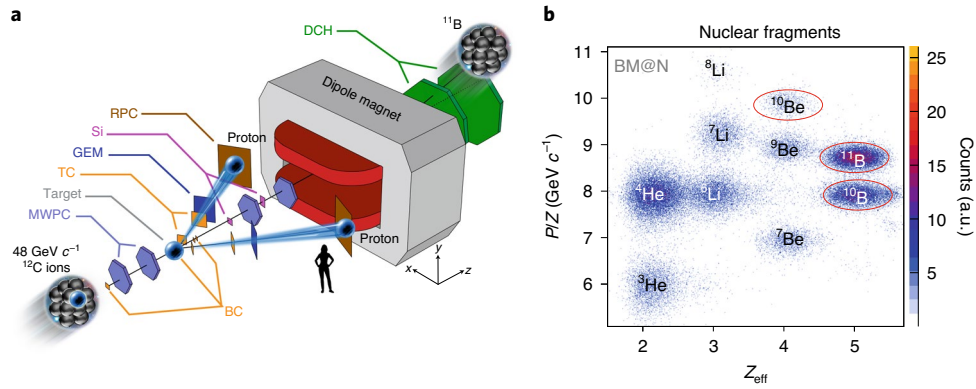
Fig. 1 | Experimental setup and fragment identification. a, Carbon nuclei travelling at 48 GeV c^{-1} hit protons in a liquid-hydrogen target, knocking out individual protons from the beam ion. Position- and time-sensitive detectors, including MWPC, GEM, RPC, Si trackers and DCH, are used to track the incoming ion beam, knockout protons and residual nuclear fragments, as well as determine their momenta. Signals from scintillator-based TCs and BCs are used to identify an interaction and record the detector data. **b**, The bend of the nuclear fragments in the large dipole magnet indicates the fragment magnetic rigidity P/Z, which—combined with the effective charge Z_{eff} measured by the BCs—allows identification of the various fragments. In this work, we refer to events with the detected ^{11}B, ^{10}B and ^{10}Be heavy fragments; see the text for details.

The experiment took place at the Joint Institute for Nuclear Research (JINR) using a 4 GeV c^{-1} per nucleon ion beam from the Nuclotron accelerator, a stationary liquid-hydrogen target, and a modified Baryonic Matter at Nuclotron (BM@N) experimental setup, as shown in Fig. 1a.

The beam was monitored upstream of the target using thin scintillator-based beam counters (BCs) used for charge identification (Extended Data Fig. 1), a veto BC for beam-halo rejection and two multiwire proportional chambers (MWPCs) for event-by-event beam tracking. The BC closer to the target was also used to define the event start time t_0.

A two-arm spectrometer (TAS) was placed downstream of the target to detect the two protons from the $(p, 2p)$ reaction that emerge between 24° and 37°, corresponding to 90° QE scattering in the two-protons centre-of-mass (c.m.) frame. Each spectrometer arm consisted of two scintillator trigger counters (TCs), a gas electron multiplier (GEM) station and a multigap resistive plate chamber (RPC) wall.

Proton tracks were reconstructed using their hit location in the GEM and RPC walls. We only consider events where the distance of closest approach between the proton tracks is smaller than 4 cm and the interaction vertex of each proton is reconstructed within the central 26 cm of the target (Extended Data Fig. 2). The time difference between the RPC and t_0 signals define the proton time of flight (TOF), which is used to determine its momentum from the measured track length, assuming a proton mass.

As the protons of interest for our analysis have momenta between 1.5 and 2.5 GeV c^{-1} ($0.85 < \beta < 0.935$), we conservatively reject events with proton tracks having $\beta > 0.96$ or $\beta < 0.8$.

Signals from the TC were combined with the BCs upstream of the target to form the main ^{12}C$(p, 2p)$ reaction trigger for the experiment. Additional triggers were set up for monitoring and calibration purposes. See Supplementary Information for details.

Nuclear fragments following the $(p, 2p)$ reaction are emitted with momentum similar to the nuclear beam momentum and at small angles with respect to the incident beam. Three silicon (Si) planes and two MWPCs were placed in the beamline downstream of the target to measure the fragment scattering angle. Following the MWPCs, the fragments enter a dipole magnet with a large acceptance of 2.87 T · m. Two drift chambers (DCHs) are used to measure the fragment trajectory after the magnet.

The fragment momenta are determined from their measured trajectories through the dipole magnet. Fragments are identified

from the combination of their rigidity (P/Z) in the magnet and energy deposition in the two scintillator-based BCs placed between the target and magnet entrance (Fig. 1b). The latter is proportional to the sum of all fragment charges squared ($Z_{eff} = \sqrt{\sum Z^2}$).

Supplementary Information provides additional details on the experimental setup and data analysis procedures.

We identify exclusive ^{12}C$(p, 2p)^{11}$B events by requiring the detection of a ^{11}B fragment in coincidence with two charged particle tracks in the TAS. Energy and momentum conservation for this reaction can be expressed as

$$\bar{\mathbf{p}}_{^{12}C} + \bar{\mathbf{p}}_{tg} = \bar{\mathbf{p}}_1 + \bar{\mathbf{p}}_2 + \bar{\mathbf{p}}_{^{11}B}, \tag{1}$$

where $\bar{\mathbf{p}}_{^{12}C} = (\sqrt{(\mathbf{p}_{^{12}C}^2 + m_{^{12}C}^2)}, 0, 0, p_{^{12}C})$ and $\bar{\mathbf{p}}_{tg} = (m_p, 0, 0, 0)$ are the incident beam ion and target proton four-momentum vectors, respectively. Here $\bar{\mathbf{p}}_1$, $\bar{\mathbf{p}}_2$ and $\bar{\mathbf{p}}_{^{11}B}$ are the four-momentum vectors of the detected protons and ^{11}B fragment. Assuming QE scattering off a nucleon moving in a mean-field potential, we can approximate $\bar{\mathbf{p}}_{^{12}C} = \bar{\mathbf{p}}_i + \bar{\mathbf{p}}_{^{11}B}$, where $\bar{\mathbf{p}}_i$ is the initial proton four-momentum inside the ^{12}C ion. Substituting this into equation (1), we obtain

$$\bar{\mathbf{p}}_i \approx \bar{\mathbf{p}}_{miss} \equiv \bar{\mathbf{p}}_1 + \bar{\mathbf{p}}_2 - \bar{\mathbf{p}}_{tg}, \tag{2}$$

where $\bar{\mathbf{p}}_{miss}$ is the measured missing four-momentum of the reaction and is only equal to $\bar{\mathbf{p}}_i$ in the case of unperturbed (no ISI/FSI) QE scattering. Throughout the text, the missing-momentum vector is shown and discussed after being boosted from the lab frame to the incident ^{12}C-ion rest frame.

Figure 2 shows the measured missing-energy distribution, $E_{miss} \equiv m_p - e_{miss}$ (where e_{miss} is the energy component of $\bar{\mathbf{p}}_{miss}$ in the ^{12}C rest frame), and its correlation with the lab-frame two-proton in-plane opening angle, $\theta_1 + \theta_2$, for inclusive ^{12}C$(p, 2p)$ (left) and exclusive ^{12}C$(p, 2p)^{11}$B (right) events. Both distributions show two distinct regions: (1) low missing energy and large in-plane opening angles that correspond to QE scattering and (2) high missing energy and small in-plane opening angles that correspond to IE scattering.

As seen in the E_{miss} projections, the inclusive ^{12}C$(p, 2p)$ events are contaminated by ISI/FSI backgrounds around and underlying both IE and QE regions that distort their distribution. This background is not evident in the ^{12}C$(p, 2p)^{11}$B case, which is the first indication that requiring the coincidence detection of ^{11}B fragments selects a unique
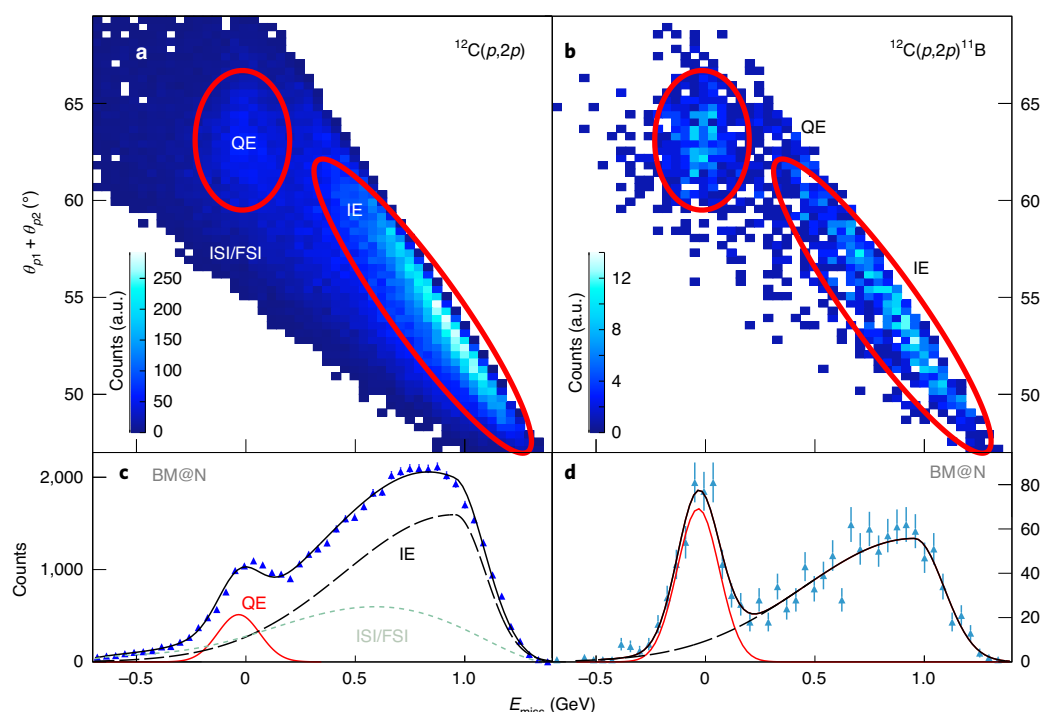
Fig. 2 | Quasi-free scattering distributions. a,b, Correlation between the measured missing energy (E_{miss}, calculated in the ^{12}C rest frame) and lab-frame two-proton in-plane opening angle ($\theta_{p1} + \theta_{p2}$). Distributions are shown for inclusive ^{12}C($p,2p$) events (**a**) and exclusive ^{12}C($p,2p$)^{11}B events (**b**). **c,d,** One-dimensional projections of the missing-energy distributions. Blue triangles show inclusive events in **c** and teal triangles show exclusive events in **d** (see Extended Data Fig. 4a for opening-angle projections). Data error bars show statistical uncertainties of the data at the 1σ confidence level. The solid red and dashed black lines show the results of a fit to the measured QE and IE peaks, respectively, using the same functional form for the distributions of both inclusive and exclusive events. The inclusive distribution requires an additional fit component—associated with ISI/FSI distortions (fine dashed green line)—to fully describe the data. QE events can be seen as a peak around the low missing energy and opening angles of ~63°. IE reactions populate the higher missing energy and lower opening angles, while ISI/FSI populate both regions and the ridge between them in the inclusive spectra.

subset of one-step processes where a single nucleon is knocked out without any further interaction with the residual fragment. We note that while the bound excited states cannot be separated from the ground state in ^{12}C($p,2p$)^{11}B events, their contribution is small[24] and should not impact the measured momentum distribution. See Supplementary Information for details.

Figure 3a shows further evidence for ISI/FSI distortion suppression by comparing the measured missing-momentum distribution for ^{12}C($p,2p$) QE events with and without ^{11}B tagging. The QE selection was done using the missing energy and in-plane opening-angle cuts depicted in Fig. 2 following a 2σ selection (see Supplementary Materials for details and Extended Data Fig. 3). The measured ^{12}C($p,2p$) QE events show a notable high-momentum tail that extends well beyond the nuclear Fermi momentum (~250 MeV c^{-1}) and is a characteristic of ISI/FSI[9]. This tail is completely suppressed by ^{11}B detection.

Figure 3b compares the measured ^{11}B momentum distribution in the ^{12}C rest frame for both QE and IE ^{12}C($p,2p$)^{11}B events. The fragment momentum distribution is equal for both reactions. This shows that the observation of a bound fragment selects quasi-free unperturbed single-step reactions, even in the case of hard IE nucleon–nucleon scattering and in a kinematical region that is otherwise dominated by FSI events.

In true unperturbed single-step ^{12}C($p,2p$)^{11}B QE scattering, the measured missing and fragment momenta should balance each other. Figure 3c shows the distribution of the cosine of the opening angle γ between the missing and fragment momenta in the plane transverse to the incident ion beam (which is insensitive to boost effects and is measured with better resolution). While broadened

due to detector resolutions, a clear back-to-back correlation is observed, which is a distinct signature of QE reactions.

The data shown in Fig. 3 are compared to the theoretical calculations of QE ($p,2p$) scattering off a p-shell nucleon in ^{12}C. The calculation is implemented via a simulation that accounts for the experimental acceptance and detector resolutions, uses measured ^{1}H($p,2p$) elastic scattering cross-section and does not include ISI/FSI effects. The total simulated event yield was scaled to match the data. See Supplementary Information for details. The calculation agrees well with all the measured ^{12}C($p,2p$)^{11}B distributions, including the fragment momentum distribution for IE events and the distribution of the angle between the missing and fragment momenta (including its tail induced by the detector resolution).

Additional data–theory comparisons are shown in Extended Data Figs. 4 and 5, which are in good agreement. This is a clear indication that ^{11}B detection strongly suppresses ISI/FSI kinematical distortions, providing access to the ground-state properties of ^{12}C.

We thus conclude that the ^{12}C($p,2p$)^{11}B QE reaction predominantly includes contributions from the single-step scattering off the p-shell protons. This is in contrast to the measured ^{12}C($p,2p$) QE reaction that includes contributions from both single-step (off p- and s-shell protons) and multistep scattering. The latter create 'QE-like' multistep scattering events that pass the QE selection, but lead to notable kinematical distortion as seen by the high missing-momentum tail (Fig. 3a). Other multistep scattering events that do not pass the QE selection lead to flux reduction.

To estimate the fractional contribution of such QE-like multiple scattering processes to the total ^{12}C($p,2p$) QE reaction cross-section, we employ a Glauber approximation calculation of the fraction
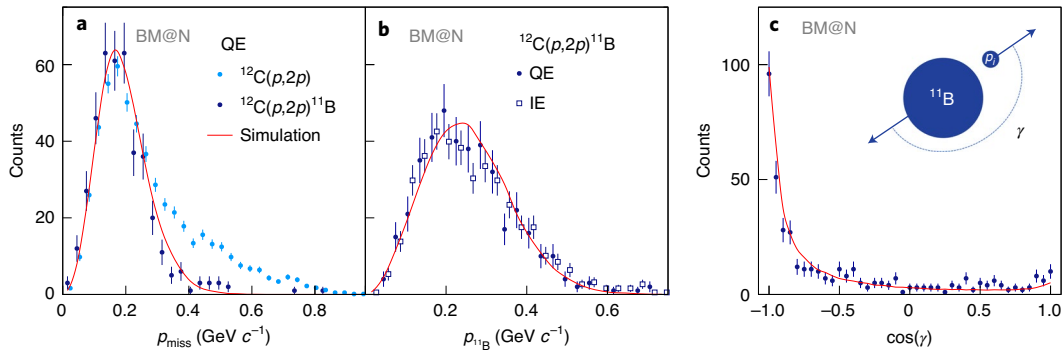
Fig. 3 | Momentum distributions and angular correlation. a, Missing-momentum (p_{miss}) distribution in the ^{12}C rest frame for QE ^{12}C($p, 2p$) and ^{12}C($p, 2p$)^{11}B events. **b**, ^{11}B fragment momentum distribution ($p_{^{11}B}$) in the ^{12}C rest frame for QE and IE ^{12}C($p, 2p$)^{11}B events. The light blue points in **a** and the open symbols in **b** have a small artificial offset of 9 and 12 MeV c^{-1}, respectively, in the positive x-axis direction for better visibility. **c**, Distribution of the cosine of the opening angle between the missing and fragment momentum in the plane transverse to the beam, namely, cos(γ). The solid red lines show the result of our QE reaction simulation. Data error bars show statistical uncertainties at the 1σ confidence level. The y axis shows the counts for the QE distribution. The IE distributions are normalized to the peak region of the QE distribution. All the variables are shown in the ^{12}C rest frame.

of single-step scattering reactions[25]. Extended Data Fig. 6 shows that the Glauber calculation effectively reproduces the measured ^{12}C($p, 2p$)^{11}B QE reaction missing-momentum distribution, but fails to do the same for the measured inclusive ^{12}C($p, 2p$) QE reaction composed of QE-like multistep processes that are highly model dependent and are not included in the calculation. The Glauber calculation follow the procedure mentioned in ref. [25]. They predict a negligible fraction of second-order multiple scattering processes (<1%) and a cross-section ratio of ^{12}C($p, 2p$)^{11}B/^{12}C($p, 2p$) single-step processes of 0.7. This calculated ratio is ~1.6 times higher than the measured ratio of $(43.7 \pm 2.4\,(\text{stat})^{+4.9}_{-5.8}\,(\text{sys}))\%$. This difference implies that the QE-like multistep processes, which are in the data but not included in the calculation, account for $37.6 \pm 8.4\%$ of the measured inclusive ^{12}C($p, 2p$) cross-section. Most of this strength is in the observed 31% enhancement in the measured ^{12}C($p, 2p$) QE event distribution at high missing momentum beyond the Glauber calculation. See Supplementary Information for details.

Thus we conclude that the ^{11}B post-selection selects single-step scattering processes, which suppresses ISI/FSI distortions that account for a large fraction of the measured ^{12}C($p, 2p$) QE reaction and are highly challenging to model. This provides access to ground-state distributions, at the price of enhanced attenuation. At high energies of the current measurement setup, this attenuation can be well modelled using Glauber calculations[25].

Next we study SRCs by measuring the ^{12}C($p, 2p$)^{10}B and ^{12}C($p, 2p$)^{10}Be reactions. SRC breakup reactions produce ^{10}B and ^{10}Be fragments when interacting with a proton–neutron (pn) or proton–proton (pp) pair, respectively. While pair breakup processes are more complex than single nucleon removal, fragment selection also helps reduce contributions by secondary scattering processes and restricts the excitation energy of the residual $A - 2$ system to below its nucleon separation energy. Furthermore, fragment detection offers a direct experimental probe for the interaction between the SRC pair nucleons and the residual $A - 2$ nucleons.

While ^{10}B and ^{10}Be fragments can be produced in the SRC breakup reaction, they can also be produced following the ($p, 2p$) interactions involving the mean-field nucleons. As discussed above, ~10% of the measured inclusive mean-field ^{12}C($p, 2p$) QE events produce excited ^{11}B fragments that decay into ^{10}B and ^{10}Be via nucleon emission. These processes can be suppressed by requiring $|\mathbf{p}_{miss}| > 350$ MeV c^{-1}, which selects protons with initial momenta that are well above the nuclear Fermi level where SRCs predominate over mean-field nucleons[13]. See Supplementary Information for details.

High $\mathbf{p}_{miss}$ ^{12}C($p, 2p$)^{10}B and ^{12}C($p, 2p$)^{10}Be events can also result from IE interactions that produce additional particles. Such reactions can involve mean-field nucleons and will not be suppressed by the high $\mathbf{p}_{miss}$ requirement. However, as shown in Fig. 2, they can be suppressed by restricting the missing energy of the reaction and requiring a large in-plane opening angle between the measured ($p, 2p$) protons.

To guide this selection, we used the generalized contact formalism (GCF)[14] to simulate ($p, 2p$) scattering events off the SRC pairs (see Supplementary Information for details). Following these calculations, we select SRC breakup reactions by requiring an in-plane opening angle larger than ~63° and $-110 \leq E_{miss} \leq 240$ MeV (Extended Data Fig. 7). We further use the total energy and momentum conservation to ensure exclusivity and suppress the IE contributions by requiring a missing nucleon mass in the entire reaction: $M^2_{miss,excl.} = (\bar{\mathbf{P}}_{^{12}C} + \bar{\mathbf{P}}_{tg} - \bar{\mathbf{P}}_1 - \bar{\mathbf{P}}_2 - \bar{\mathbf{P}}_{^{10}B(Be)})^2 \approx m_N^2$ where m_N is the nucleon mass and $M_{miss,excl.}$ is the exclusive reaction missing mass (Extended Data Fig. 8).

Applying these selection cuts, we measured twenty-three ^{12}C($p, 2p$)^{10}B and two ^{12}C($p, 2p$)^{10}Be events. The large ^{10}B/^{10}Be event yield ratio is generally consistent with the previously observed predominance of pn over pp SRC pairs[10,12,13,26,27]. This measured ratio of 11.5 ± 2.5 is in full agreement with the GCF-calculated ^{10}B/^{10}Be yield ratio of 12.1, obtained using input from ab initio many-body calculations[14]. The observed ^{10}B dominance also contradicts an expectation of similar ^{10}B and ^{10}Be yields if the measured reactions were dominated by mean-field QE scattering followed by FSI with a single nucleon in ^{11}B.

Figure 4a–c shows the missing-energy and missing-momentum distributions of the selected SRC ^{12}C($p, 2p$)^{10}B events. The measured distributions show good agreement with the GCF predictions. Additional kinematical distributions are shown and compared with the GCF in Extended Data Figs. 9 and 10. We specifically note that the distributions of the z component of the missing momentum is not centred around zero and is shifted towards the incident-beam direction (Extended Data Fig. 9c). This is expected because of the strong s dependence of the large-angle elementary pp elastic scattering cross-section. See discussion in Supplementary Information.

Next we examine the angular correlations between the nucleons in the pair and between the pair and the ^{10}B fragment. Figure 4d shows the distribution of the cosine of the angle between the missing momentum (equation (2)) and the reconstructed undetected recoil neutron momentum. A clear back-to-back correlation is observed, as expected for strongly correlated nucleon pairs. The width of the distribution is driven by the pair c.m. motion and
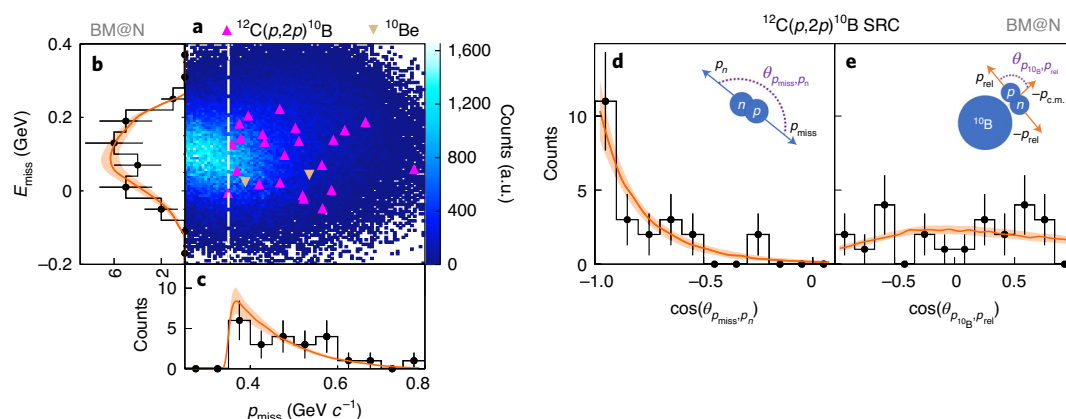
Fig. 4 | Selection of SRC breakup events and angular correlations. a, Correlation between the missing energy E_{miss} and missing momentum p_{miss} for the measured $^{12}C(p,2p)^{10}B$ (upwards-facing purple triangles) and $^{12}C(p,2p)^{10}Be$ (downwards-facing brown triangles) SRC events, on top of the GCF simulation (the colour scale is only relative as the absolute scale is set by the simulation statistics). The vertical white dashed line shows our event-selection cut of $p_{miss} \geq 350\,MeV\,c^{-1}$. **b–e**, One-dimensional distributions of the measured (black points) and GCF-simulated (orange line) $^{12}C(p,2p)^{10}B$ events as a function of the missing energy (**b**), missing momentum (**c**), cosine of the angle between the recoil nucleon and missing momentum $\cos(\theta_{p_{miss},p_n})$ (**d**) and angle between the ^{10}B fragment and pair relative momentum $\cos(\theta_{p_{10B},p_{rel}})$ (**e**). The width of the orange bands and the data error bars show the systematic uncertainties of the model and the data statistical uncertainties, respectively, each at the 1σ confidence level.

detection resolutions. It shows good agreement with the GCF prediction that assumes a three-dimensional Gaussian c.m. momentum distribution[14,28].

An independent determination of the SRC pair c.m. momentum distribution can be obtained from the ^{10}B momentum distribution that is measured here (Extended Data Fig. 9e–h). From these data, we extract an SRC pair c.m. momentum distribution with a Gaussian width of $\sigma_{c.m.} = (156 \pm 27)\,MeV\,c^{-1}$ (see Supplementary Information for extraction details), which is in agreement with previous electron scattering measurements[28].

Last, we examine the factorization of the measured SRC pairs from the residual nuclear system. The strong two-body interaction between the nucleons in the pair was predicted[9,14,23] to allow modelling its distribution as independent functions of the pair relative and c.m. motion, with no correlation between them. Such factorization dramatically simplifies the SRC calculations and should be evident experimentally by a lack of correlation between the pair c.m. and relative momenta.

Figure 4e shows the distribution of the cosine of the angle between the ^{10}B fragment momentum (that is, pair c.m. momentum) and the pair relative momentum given by $p_{rel} = (p_{miss} - p_n)/2$, where p_n is the reconstructed recoil neutron momenta. The GCF assumes the above-mentioned factorization and therefore predicts a flat distribution, which is slightly shaped by the acceptance of our detectors. These data are in full agreement with this assumption.

Therefore, by investigating SRC pairs with the detection of the residual-bound $A - 2$ nucleons system, we are able to provide direct experimental evidence for the factorization of SRC pairs from the many-body nuclear medium.

The dominant contributions of ISI/FSI to nucleon knockout scattering measurements have been a major difficulty for experimentally extracting nucleon distributions in the nuclei[9,13,29–31]. Even in high-energy electron scattering at selected kinematics that minimize their contributions, the remaining FSI effects lead to attenuation, which is effectively modelled theoretically[25], and distortions whose modelling is more challenging and introduce an interpretation uncertainty to the obtained results, especially at large missing momentum[9,13,31,32].

At lower beam energies, the method of quasi-free proton-induced nucleon knockout in inverse kinematics has been recently

developed and applied to study the single-particle structure of exotic nuclei[4,5,22,24]. The data analysis and interpretation of these results heavily relies on the assumption that the extracted particle distributions are free from FSI distortions, for both QE and IE reactions, which has not been experimentally proven to date.

Our findings, however, clearly demonstrate the feasibility of accessing properties of single nucleons and SRC nucleon pairs in short-lived nuclei, particularly neutron-rich nuclei, using high-energy radioactive beams, produced at upcoming accelerator facilities such as Facility for Rare Isotope Beams (FRIB) and Facility for Antiproton and Ion Research (FAIR). With this method, we accomplished a big step towards realizing the goal of such facilities, which is exploring the formation of visible matter in the Universe in the laboratory. The presented experimental method thus provides a basis to approximate—as closely as possible—the dense, cold neutron-rich matter in neutron stars in the laboratory.

Online content

Any methods, additional references, Nature Research reporting summaries, source data, extended data, supplementary information, acknowledgements, peer review information; details of author contributions and competing interests; and statements of data and code availability are available at https://doi.org/10.1038/s41567-021-01193-4.

References

1. Jacob, G. & Maris, T. A. J. Quasi-free scattering and nuclear structure. *Rev. Mod. Phys.* **38**, 121–142 (1966).
2. Kelly, J. J. Nucleon knockout by intermediate energy electrons. *Adv. Nucl. Phys.* **23**, 75–294 (1996).
3. Gade, A. et al. Reduction of spectroscopic strength: weakly-bound and strongly-bound single-particle states studied using one-nucleon knockout reactions. *Phys. Rev. C* **77**, 044306 (2008).
4. Kobayashi, T. et al. (*p,2p*) reactions on ^{9-16}C at 250 MeV/A. *Nucl. Phys. A* **805**, 431–438 (2008).
5. Wakasa, T., Ogata, K. & Noro, T. Proton-induced knockout reactions with polarized and unpolarized beams. *Prog. Part. Nucl. Phys.* **96**, 32–87 (2017).
6. Duer, M. et al. Probing high-momentum protons and neutrons in neutron-rich nuclei. *Nature* **560**, 617–621 (2018).

7. Hansen, P. G. & Tostevin, J. A. Direct reactions with exotic nuclei. *Ann. Rev. Nucl. Part. Sci.* **53**, 219–261 (2003).

8. Cosyn, W. & Ryckebusch, J. On the density dependence of single-proton and two-proton knockout reactions under quasifree conditions. *Phys. Rev. C* **80**, 011602 (2009).

9. Ciofi degli Atti, C. In-medium short-range dynamics of nucleons: recent theoretical and experimental advances. *Phys. Rep.* **590**, 1–85 (2015).

10. Subedi, R. et al. Probing cold dense nuclear matter. *Science* **320**, 1476–1478 (2008).

11. Feldmeier, H., Horiuchi, W., Neff, T. & Suzuki, Y. Universality of short-range nucleon-nucleon correlations. *Phys. Rev. C* **84**, 054003 (2011).

12. Hen, O. et al. Momentum sharing in imbalanced Fermi systems. *Science* **346**, 614–617 (2014).

13. Hen, O., Miller, G. A., Piasetzky, E. & Weinstein, L. B. Nucleon-nucleon correlations, short-lived excitations, and the quarks within. *Rev. Mod. Phys.* **89**, 045002 (2017).

14. Cruz-Torres, R. et al. Many-body factorization and position–momentum equivalence of nuclear short-range correlations. *Nat. Phys.* https://doi.org/10.1038/s41567-020-01053-7 (2020).

15. Spiller, P. & Franchetti, G. The FAIR accelerator project at GSI. *Nucl. Instrum. Meth. A* **561**, 305–309 (2006).

16. *FRIB400: The Scientific Case for the 400 MeV/u Energy Upgrade of FRIB* (FRIB Science Community, 2019); https://frib.msu.edu/_files/pdfs/frib400_final.pdf

17. Mukherjee, B. et al. Spectral response and contact of the unitary Fermi gas. *Phys. Rev. Lett.* **122**, 203402 (2019).

18. Bloch, I., Dalibard, J. & Zwerger, W. Many-body physics with ultracold gases. *Rev. Mod. Phys.* **80**, 885–964 (2008).

19. Schmidt, A. et al. Probing the core of the strong nuclear interaction. *Nature* **578**, 540–544 (2020).

20. Cruz-Torres, R. et al. Probing few-body nuclear dynamics via ³H and ³He (e,e'p)pn cross-section measurements. *Phys. Rev. Lett.* **124**, 212501 (2020).

21. Obertelli, A. & Uesaka, T. Hydrogen targets for exotic-nuclei studies developed over the past 10 years. *Eur. Phys. J. A* **47**, 105 (2011).

22. Atar, L. et al. Quasifree (p,2p) reactions on oxygen isotopes: observation of isospin independence of the reduced single-particle strength. *Phys. Rev. Lett.* **120**, 052501 (2018).

23. Chen, J.-W., Detmold, W., Lynn, J. E. & Schwenk, A. Short range correlations and the EMC effect in effective field theory. *Phys. Rev. Lett.* **119**, 262502 (2017).

24. Panin, V. et al. Exclusive measurements of quasi-free proton scattering reactions in inverse and complete kinematics. *Phys. Lett. B* **753**, 204–210 (2016).

25. Aumann, T., Bertulani, C. A. & Ryckebusch, J. Quasifree (p,2p) and (p,pn) reactions with unstable nuclei. *Phys. Rev. C* **88**, 064610 (2013).

26. Piasetzky, E., Sargsian, M., Frankfurt, L., Strikman, M. & Watson, J. W. Evidence for strong dominance of proton-neutron correlations in nuclei. *Phys. Rev. Lett.* **97**, 162504 (2006).

27. Duer, M. et al. Direct observation of proton-neutron short-range correlation dominance in heavy nuclei. *Phys. Rev. Lett.* **122**, 172502 (2019).

28. Cohen, E. O. et al. Center of mass motion of short-range correlated nucleon pairs studied via the A(e,e'pp) reaction. *Phys. Rev. Lett.* **121**, 092501 (2018).

29. Bobeldijk, I. et al. High-momentum protons in ²⁰⁸Pb. *Phys. Rev. Lett.* **73**, 2684–2687 (1994).

30. Blomqvist, K. I. et al. Investigation of short-range nucleon-nucleon correlations using the reaction ¹²C(e,e'pp) in close to 4π geometry. *Phys. Lett. B* **421**, 71–78 (1998).

31. Benmokhtar, F. et al. Measurement of the ³He(e,e'p)pn reaction at high missing energies and momenta. *Phys. Rev. Lett.* **94**, 082305 (2005).

32. Frankfurt, L., Sargsian, M. & Strikman, M. Recent observation of short-range nucleon correlations in nuclei and their implications for the structure of nuclei and neutron stars. *Int. J. Mod. Phys. A* **23**, 2991–3055 (2008).

The BM@N Collaboration

M. Patsyuk[1,2], J. Kahlbow[1,3], G. Laskaris[1,3], M. Duer[4], V. Lenivenko[2], E. P. Segarra[1], T. Atovullaev[2,5], G. Johansson[3], T. Aumann[4,6,7], A. Corsi[8], O. Hen[1], M. Kapishin[2], V. Panin[6,8], E. Piasetzky[3], Kh. Abraamyan[2], S. Afanasiev[2], G. Agakishiev[2], P. Alekseev[9], E. Atkin[10], T. Aushev[11], V. Babkin[2], V. Balandin[2], D. Baranov[2], N. Barbashina[10], P. Batyuk[2], S. Bazylev[2], A. Beck[1], C. A. Bertulani[12], D. Blaschke[13], D. Blau[14], D. Bogoslovsky[2], A. Bolozdynya[10], K. Boretzky[6], V. Burtsev[2], M. Buryakov[2], S. Buzin[2], A. Chebotov[2], J. Chen[15], A. Ciszewski[13], R. Cruz-Torres[1], B. Dabrowska[2], D. Dabrowski[2,16], A. Dmitriev[2], A. Dryablov[2], P. Dulov[2], D. Egorov[2], A. Fediunin[2], I. Filippov[2], K. Filippov[10], D. Finogeev[10,17], I. Gabdrakhmanov[2], A. Galavanov[2,10], I. Gasparic[18], O. Gavrischuk[2], K. Gertsenberger[2], V. Golovatyuk[2], M. Golubeva[17], F. Guber[11,17], Yu. Ivanova[2], A. Ivashkin[11,17], A. Izvestnyy[17], S. Kakurin[2], V. Karjavin[2], N. Karpushkin[17], R. Kattabekov[2], V. Kekelidze[2], S. Khabarov[2], Yu. Kiryushin[2], A. Kisiel[16], V. Kolesnikov[2], A. Kolozhvari[2], Yu. Kopylov[2], I. Korover[3], L. Kovachev[2,19], A. Kovalenko[2], Yu. Kovalev[2], A. Kugler[20], S. Kuklin[2], E. Kulish[2], A. Kuznetsov[2], E. Ladygin[2], N. Lashmanov[2], E. Litvinenko[2], S. Lobastov[2], B. Löher[4], Y.-G. Ma[15], A. Makankin[2], A. Maksymchuk[2], A. Malakhov[2], I. Mardor[3], S. Merts[2], A. Morozov[2], S. Morozov[10,17], G. Musulmanbekov[2], R. Nagdasev[2], D. Nikitin[2], V. Palchik[2], D. Peresunko[14], M. Peryt[2], O. Petukhov[17], Yu. Petukhov[2], S. Piyadin[2], V. Plotnikov[2], G. Pokatashkin[2], Yu. Potrebenikov[2], O. Rogachevsky[2], V. Rogov[2], K. Rosłon[2,16], D. Rossi[4], I. Rufanov[2], P. Rukoyatkin[2], M. Rumyantsev[2], D. Sakulin[2], V. Samsonov[10], H. Scheit[4], A. Schmidt[1], S. Sedykh[2], I. Selyuzhenkov[10], P. Senger[10], S. Sergeev[2], A. Shchipunov[2], A. Sheremeteva[2], M. Shitenkov[2], V. Shumikhin[10], A. Shutov[2], V. Shutov[2], H. Simon[6], I. Slepnev[2], V. Slepnev[2], I. Slepov[2], A. Sorin[2], V. Sosnovtsev[10], V. Spaskov[2], T. Starecki[16], A. Stavinskiy[9], E. Streletskaya[2], O. Streltsova[2], M. Strikhanov[10], N. Sukhov[2], D. Suvarieva[2], J. Tanaka[4], A. Taranenko[10], N. Tarasov[2], O. Tarasov[2], V. Tarasov[9], A. Terletsky[2],

O. Teryaev[2], V. Tcholakov[19], V. Tikhomirov[2], A. Timoshenko[2], N. Topilin[2], B. Topko[2], H. Törnqvist[4], I. Tyapkin[2], V. Vasendina[2], A. Vishnevsky[2], N. Voytishin[2], V. Wagner[4], O. Warmusz[13], I. Yaron[3], V. Yurevich[2], N. Zamiatin[2], Song Zhang[15], E. Zherebtsova[17], V. Zhezher[2], N. Zhigareva[9], A. Zinchenko[2], E. Zubarev[2] and M. Zuev[2]

[9]Institute for Theoretical and Experimental Physics (ITEP), Moscow, Russia. [10]National Research Nuclear University MEPhI, Moscow, Russia. [11]Moscow Institute of Physics and Technology (MIPT), Moscow, Russia. [12]Texas A&M University—Commerce, Commerce, TX, USA. [13]University of Wrocław, Wroclaw, Poland. [14]Kurchatov Institute, Moscow, Russia. [15]Key Laboratory of Nuclear Physics and Ion-Beam Application (MOE), Institute of Modern Physics, Fudan University, Shanghai, China. [16]Warsaw University of Technology, Warsaw, Poland. [17]Institute for Nuclear Research of the Russian Academy of Sciences (INR RAS), Moscow, Russia. [18]Rudjer Boskovic Institute, Zagreb, Croatia. [19]Nuclear Physics Institute, CAS, Rež, Czech Republic. [20]Plovdiv University 'Paisii Hilendarski', Plovdiv, Bulgaria.

Methods

Ion beam. The primary beam ions were produced in a KRION source and accelerated in the Nuclotron[33], quasi-continuously delivering pulses for 2 s followed by 8 s pauses between spills. Each pulse delivered 2.5×10^5 ions on average.

The beam contained a mixture of ^{12}C, ^{14}N and ^{16}O ions with average fractions of 68%, 18% and 14%, respectively. The ^{12}C ions have a beam momentum of 3.98 GeV $c^{-1} u^{-1}$ (where u stands for nucleon number) at the centre of the LH$_2$ target. They are focused on the target with a beam diameter of about 4 cm (Extended Data Fig. 2c).

The beam ions are identified on an event-by-event basis using their energy loss in the scintillator-based BCs (BC1 and BC2 upstream of the target), which is proportional to the square of their nuclear charge, Z^2. The selection of the incoming nuclear species is shown in Extended Data Fig. 1. Pile-up events are rejected by checking the multiplicity of the BC2 time signal.

Detectors upstream of the target. Before hitting the target, the beam was monitored by the two thin scintillator-based BCs (namely, BC1 and BC2) and two MWPCs mentioned above. The MWPCs determined the incident-beam-ion trajectory for each event. Besides using the energy deposition in the BCs for beam-ion identification, the BC closer to the target was read by a fast microchannel plates photomultiplier tube used to define the event start time t_0. Beam-halo interactions were suppressed using a dedicated BC veto counter consisting of a scintillator with a hole of 5 cm diameter at its centre.

Liquid-hydrogen target. The target[34] was cryogenically cooled and the hydrogen was recondensated using liquid helium. The liquid hydrogen was held at 20 K and 1.1 atm in a 30-cm-long 6-cm-diameter aluminized Mylar cylindrical container. The container entrance and exit windows were made out of 110-μm-thick Mylar. The target constitutes a 14% interaction length for ^{12}C. A sketch of the target cell is shown in Extended Data Fig. 2.

TAS. A TAS was placed downstream of the target and was used to detect the two protons from the $(p, 2p)$ reaction that emerge between 24° and 37°. The vertical acceptance of each arm is ±7°. These laboratory scattering angles correspond to ~90° (75–101°) QE scattering in the two-proton c.m. frame. Each spectrometer arm consisted of scintillator TCs, GEM stations and multigap RPC walls.

The proton tracks are formed using their hit locations in the GEM and RPC walls. The vertex resolution along the beamline direction is 1.8 cm (1σ) and was measured using a triple lead foil target, as detailed in the Supplementary Information.

The time difference between the RPC and t_0 signals defines the proton TOF. The TOF—combined with the measured track length (accounting for the exact interaction vertex in the target)—is used to determine its momentum. The measurements of gamma rays from the interactions with a single lead foil target were used for absolute TOF calibration. An absolute TOF resolution of 175 ps was extracted, which dominates the momentum resolution (see Supplementary Information for details).

Reaction vertex and proton identification. The z position (along the beamline) of the reaction vertex is reconstructed from two tracks in the TAS, while the (x, y) position is obtained from the extrapolated MWPC track in front of the target (the latter provides a better transverse position resolution). Details about the algorithm and performance can be found in the Supplementary Information.

The reconstructed vertex position along the beamline and transverse to it with the inserted liquid-hydrogen target is shown in Extended Data Fig. 2. The structure of the target—the LH$_2$ volume and other in-beam materials, such as the target walls, styrofoam cover and various isolation foils—is well reconstructed. The vertex quality is ensured by requiring that the minimum distance between the two tracks, which define the vertex, is smaller than 4 cm. In addition, we place a selection on the absolute z vertex, requiring it to be reconstructed within ±13 cm from the centre of the target.

Scattering from the target vessel that was not rejected by the veto counter is removed by a cut on the (x, y)-vertex direction. This removes a strong peak due to the styrofoam cover over the target (Extended Data Fig. 2c).

After determining the tracks and the vertex, the momentum of each proton is calculated with respect to the incoming-beam direction by using the TOF information between the target and the RPC.

To select $(p, 2p)$ events from quasi-free scattering, other particles that also create a track but originate from IE reactions (mostly pions) need to be rejected. We apply several criteria (outlined in the next section), but the basic selection is a cut to the velocity of the two measured particles, as shown in Supplementary Fig. 4b. In the analysis, both particles detected in the TAS must pass the velocity condition of $0.80 < \beta < 0.96$, removing fast and slow pions.

Fragment detection. Nuclear fragments following the $(p, 2p)$ reaction are emitted at small angles with respect to the incident beam with momentum that is similar to the beam momentum. To measure the fragment scattering angle, three Si planes and two MWPCs are placed in the beamline downstream of the target. Following the MWPCs, the fragments enter a dipole magnet with a large acceptance of 2.87 T·m, and they are bent according to their momentum-to-charge ratio (P/Z),

namely, the magnetic rigidity. Two large-acceptance DCHs with eight wire planes each are used to measure the fragment trajectory after the magnet.

The fragment momenta are determined from the measurement of their bending angle in the magnet. Fragment identification (nuclear mass and charge) is done using their bend in the magnetic field and energy deposition in two scintillator-based BCs (BC3 and BC4) placed between the target and magnet entrance (Fig. 1b). The latter is proportional to the sum of all the squared fragment charges, namely, $Z_{\text{eff}} \equiv \sqrt{\sum Z^2}$.

Fragment momentum and identification. We follow a simulation-based approach to derive P/Z from a multidimensional fit to the measured fragment trajectories before and after the magnet. The particle trajectory is determined using the MWPC–Si track before the magnet and the DCH track after the magnet. Both tracks serve as input for the P/Z determination.

The momentum resolution was determined using unreacted ^{12}C beam ions (from empty-target runs) and found to be equal to 0.78 GeV c^{-1} (1.6%) (Supplementary Fig. 2). This resolution is consistent with the resolution expected from events obtained with simulation that accounts for the incoming-beam energy spread. Using beam-trigger events (Supplementary Information), we verified that the momentum reconstruction resolution is the same when ^{12}C ions go through a full liquid-hydrogen target. The achieved momentum accuracy is evaluated from simulation to be equal to 0.2%.

The fragment-tracking efficiency, including the detection efficiency of the upstream MWPC–Si, downstream DCH detectors, and track reconstruction and selection algorithm, equals ~40%. See Supplementary Information for details on the tracking algorithms and its performance.

Figure 1b illustrates an example of this fragment identification from the experimental data using P/Z obtained by the multidimensional fit versus the total charge measured in the scintillators.

This work only focuses on fragments with a nuclear charge of 4 or larger, with a single track matched between the upstream and downstream tracks. Although the charge of the fragments is only measured as an integrated signal in BC3 and BC4, the boron isotopes can be unambiguously selected since no possible combination of fragments could otherwise mimic a signal amplitude proportional to $\sum Z^2 = 25$. In the case of ^{10}Be, the only other fragment of interest here with $Z_{\text{eff}} = 4$ is contamination from within the resolution and it is excluded by using the additional P/Z information. Further, ^{10}Be is the only possible fragment with $P/Z \approx 10$ GeV c^{-1} in this region and is well separated.

Besides requiring a good vertex and single global-track events, we employ Z_{eff} and P/Z selection criteria to identify ^{11}B, ^{10}B or ^{10}Be. A two-dimensional charge selection—as for the incoming charge—was applied here for BC3 and BC4. Even for the selection in P/Z versus Z_{eff}, a two-dimensional cut was applied, as indicated in Fig. 1b, with a $\approx 2\sigma$ selection in P/Z.

Detection efficiencies of single heavy fragments. As discussed above, this work is limited to reactions with a single heavy ($Z \geq 4$) fragment in the final state. The detection of such a fragment depends on the ability of the fragment to emerge from the liquid-hydrogen target without re-interacting, as well as our ability to identify its charge in the two BCs downstream of the target, and reconstruct its tracks before and after the magnet.

We extract the efficiencies for the charge and track reconstruction using the beam-only data (that is, no target vessel in the beamline). We assume that within the quoted uncertainties below, there is no difference between the efficiencies for detecting $Z = 6$ and $Z = 5$ and 4 fragments.

To determine the efficiency for ascertaining the fragment's charge in the BCs downstream of the target, we first select the incident ^{12}C ions based on their energy loss in BC1 and BC2 (Extended Data Fig. 1). We then examine the fraction of those ^{12}C ions also identified by their energy loss in BC3 and BC4 downstream of the target. This fraction defines a charge identification efficiency $\epsilon_Z = (83 \pm 6)\%$, where the uncertainty is obtained from examining the different energy-deposition cuts between $2 - 3\sigma$ on the Gaussian distribution in BC3 and BC4. The standard deviation in efficiency from this cut variation relative to the mean value defines the uncertainty. The fraction of such $Z_{\text{in}} = Z_{\text{out}} = 6$ events with a single reconstructed track and $P/Z = 8$ GeV c^{-1} is equal to $(39.5^{+1.7}_{-2.6})\%$, determined in a $\pm 2.20\sigma$ range with the $\pm 0.45\sigma$ range to account for this uncertainty. In the case of ^{10}Be fragments, the tracking efficiency is $(39.5^{+5.1}_{-7.8})\%$ due to larger systematic effects. The larger asymmetry towards smaller efficiency arises from a possible background contribution in the reconstructed P/Z that is taken into account. More details are given in the next section and in the Supplementary Information, particularly about single-track identification and its efficiency.

Extracting QE ^{12}C$(p, 2p$X$)/^{12}$C$(p, 2p)$ ratios for ^{11}B, ^{10}B and ^{10}Be. To extract the fraction of $(p, 2p)$ events with a detected heavy fragment, we need to apply several corrections to the number of measured events that do not cancel in the ratio. The ratio of the exclusive cross-section with a detected fragment to the inclusive cross-section is given by

$$\frac{^{12}\text{C}(p, 2p)\text{X}}{^{12}\text{C}(p, 2p)} = \frac{R}{\epsilon_Z \times \epsilon_{\text{track}} \times \text{att}}, \tag{3}$$

where X stands for the detected fragment and

- R is the measured ratio based on the number of QE events for each sample. We added a cut on the low missing momentum, $p_{\text{miss}} < 250\,\text{MeV}\,c^{-1}$, in addition to the missing energy and in-plane opening-angle cuts to clean up the inclusive $(p, 2p)$ sample, and focusing on the region of the small missing momentum.
- ϵ_Z is the outgoing fragment charge efficiency. We consider a value of $\epsilon_Z = (83 \pm 6)\%$ (see discussion above).
- ϵ_{track} is the outgoing fragment-tracking efficiency with all the selection cuts applied in a $\pm 2.2\sigma P/Z$ range. We consider a value of $\epsilon_{\text{track}} = (39.5^{+1.7}_{-2.6})\%$ for ^{11,10}B and $\epsilon_{\text{track}} = (39.5^{+5.1}_{-7.8})\%$ for ^{10}Be (see discussion above).
- att is the attenuation of the outgoing fragment due to secondary fragmentation in the target. After the reaction, the flux of the fragment depends on the remaining distance that the fragment needs to travel in the target. The attenuation is given by the reduction of this flux

$$\text{att} = \exp(-\rho \sigma_{\text{tot}} z), \qquad (4)$$

where ρ is the target density and σ_{tot} is the total reaction cross-section. We evaluate the attenuation factor by taking an average over the 30 cm target length using $\sigma_{\text{tot}} = 220 \pm 10\,\text{mb}$ (assumed to be the same for ^{10}B and ^{10}Be within uncertainty), such that $\text{att} = 0.87 \pm 0.01$. Additional breakup reactions due to the material in the beamline downstream of the target were estimated (and scaled) based on the total cross-section on carbon. The contribution to the secondary reaction probability is comparably small, particularly reactions from ^{11}B to ^{10}B or ^{10}Be are negligible.

The total reaction cross-section σ_{tot} is calculated in eikonal reaction theory[35] using the ^{11}B harmonic-oscillator-like density distribution and the nucleon–nucleon cross-section at $4\,\text{GeV}\,c^{-1}\,\text{u}^{-1}$ as the input. In a benchmark test, it reproduces the measured cross-section for ^{11}B + ^{12}C at kinetic energy of $950\,\text{MeV}\,\text{u}^{-1}$ (ref. [36]), while the beam energy only has a very small impact. We consider the ~5% systematic overestimate of the eikonal cross-sections compared with measurements as uncertainty.

From equation (3), we see that there are four individual contributions to the uncertainty in the ratio of ^{12}C$(p, 2p$X$)/^{12}$C$(p, 2p)$: statistics ΔR, efficiencies ($\Delta \epsilon_Z$ and $\Delta \epsilon_{\text{track}}$) and attenuation ($\Delta$att). In addition, we have a systematic uncertainty due to the event-selection cuts. Each event cut was modified over a given σ range and the resulting change in the relative yield was taken as the systematic uncertainty. The 2D E_{miss}-angle cuts were varied as $(2 \pm 1/2)\sigma$, where both these quantities are described by a Gaussian. The cut in the missing momentum was varied according to the missing-momentum resolution like $p_{\text{miss}} < 250 \pm 50\,\text{MeV}\,c^{-1}$. These uncertainties are quoted as symmetric uncertainties since in the simulation we did not observe a notable asymmetry in the measured quantities. Besides that, we also consider a possible background contribution in the P/Z determination as additional asymmetric systematic uncertainty. It is determined for each charge selection separately with a fit in the shape of a second-order polynomial to the P/Z distribution under QE conditions. Since the fits with and without background contribution result in very similar goodness, we chose to adapt the possible background as 2σ uncertainty. Combining these contributions, we obtain the following fractions given with statistical (stat) and systematic (sys) uncertainties:

$$\frac{^{12}\text{C}(p,2p)^{11}\text{B}}{^{12}\text{C}(p,2p)} = (43.7 \pm 2.4\,(\text{stat})^{+4.9}_{-5.8}\,(\text{sys}))\%,$$

$$\frac{^{12}\text{C}(p,2p)^{10}\text{B}}{^{12}\text{C}(p,2p)} = (7.8 \pm 1.0\,(\text{stat})^{+1.3}_{-1.4}\,(\text{sys}))\%,$$

$$\frac{^{12}\text{C}(p,2p)^{10}\text{Be}}{^{12}\text{C}(p,2p)} = (0.9 \pm 0.4\,(\text{stat})^{+0.2}_{-0.3}\,(\text{sys}))\%.$$

Data availability
Source data are provided with this paper. All other data that support the plots within this paper and other findings of this study are available from the corresponding author upon reasonable request.

References
33. Kekelidze, V. et al. Project NICA at JINR. *Nucl. Phys. A* **904–905**, 945c–948c (2013).
34. Agapov, N. N. et al. Cryogenic targets of the lightest gases (hydrogen, deuterium and helium-4) with GM cryocooler for experiments of high energy physics. In *Cryogenics 2019. Proc. 15th IIR International Conference* 38–44 (IIF-IIR, 2019).
35. Hussein, M. S., Rego, R. A. & Bertulani, C. A. Microscopic theory of the total reaction cross section and application to stable and exotic nuclei. *Phys. Rep.* **201**, 279–334 (1991).
36. Ozawa, A., Suzuki, T. & Tanihata, I. Nuclear size and related topics. *Nucl. Phys. A* **693**, 32–62 (2001).

Author contributions
The experimental setup at the Nuclotron was designed and constructed by the BM@N Collaboration at JINR. Data reconstruction and calibration, Monte Carlo simulations of the detector and data analyses were performed by a large number of BM@N Collaboration members, who also discussed and approved the scientific results. All authors read and approved the manuscript. In particular, the design and construction of the TAS was lead by G.L., who also led the data-taking period. The development and operation of the data acquisition and trigger systems were lead by S. Basylev and V.Y., respectively. The development and operation of the GEM and silicon detectors were lead by A. Maksymchuk and N. Zamyatin, respectively. Raw data processing and online monitoring were performed by S. Merts and I. Gabdrakhmanov M.R. contributed to the RPC analysis, V. Palchik contributed to the Si/MWPC analysis, D. Baranov contributed to the GEM analysis and N.V. contributed to the DCH analysis. The main data analysis was done by J.K., M. Patsyuk, V.L., E.P.S., T.A., G.J., V.P., and M.D., with input from O.H., E.P., T. Aumann, M.K. and A. Corsi, and reviewed by the BM@N Collaboration.

Competing interests
The authors declare no competing interests.

Additional information
Extended data is available for this paper at https://doi.org/10.1038/s41567-021-01193-4.

Supplementary information The online version contains supplementary material available at https://doi.org/10.1038/s41567-021-01193-4.

Correspondence and requests for materials should be addressed to O.H.

Peer review information *Nature Physics* thanks Daniel Bazin, Olof Tengblad and the other, anonymous, reviewer(s) for their contribution to the peer review of this work.

Reprints and permissions information is available at www.nature.com/reprints.
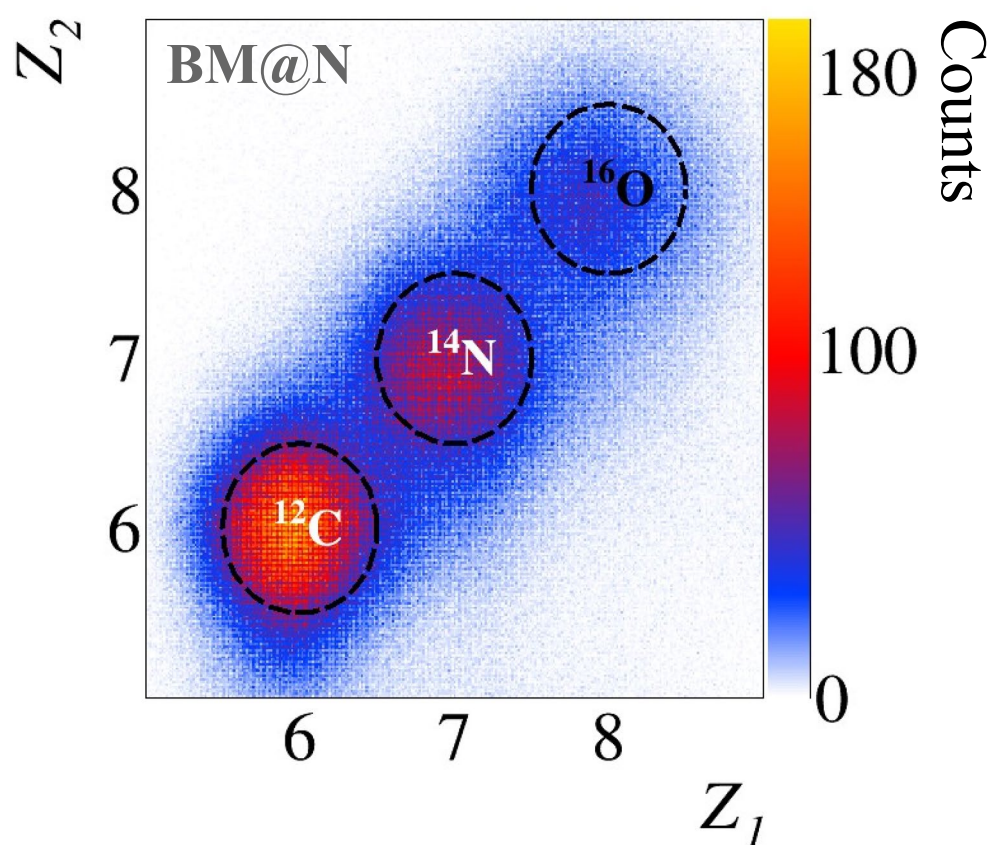
Extended Data Fig. 1 | Incoming beam ions. Charge identification of incoming beam ions measured event-wise using the two beam counters (BC1, BC2) in front of the target. Besides ^{12}C, the $A/Z = 2$ nuclei ^{14}N and ^{16}O are mixed in the beam with less intensity.
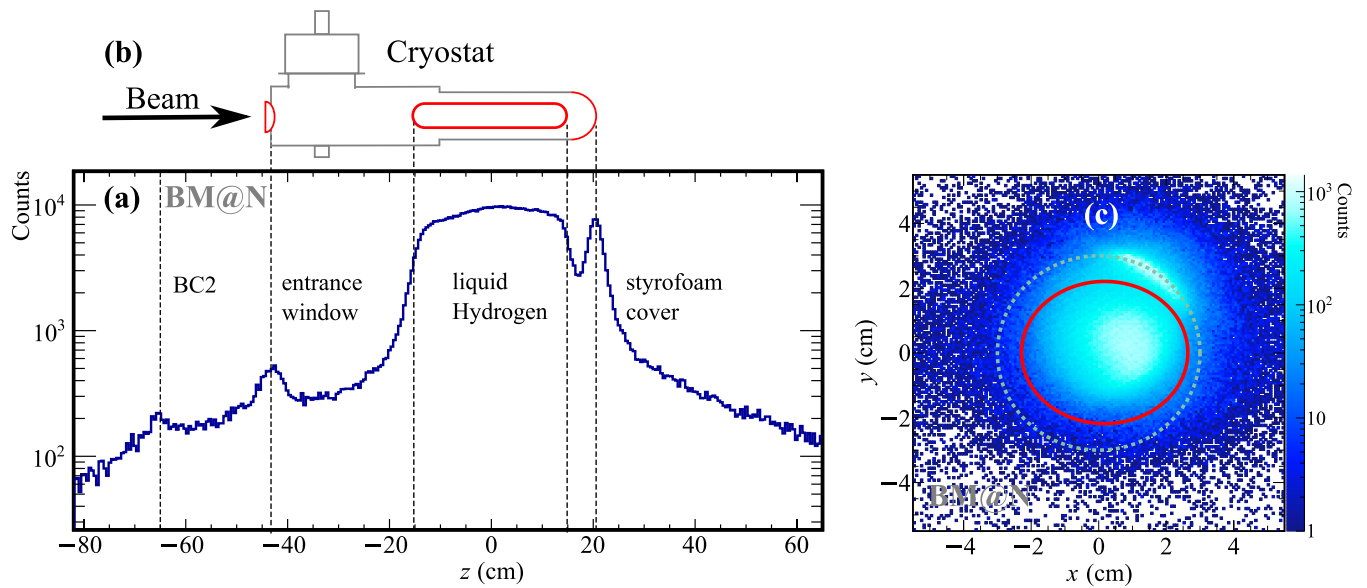
Extended Data Fig. 2 | Reaction vertex. Reconstructed reaction vertex in the LH$_2$ target. The position along the beam line is shown in (**a**), scattering off in-beam material is also visible. For comparison, a sketch of the target device is shown in (**b**). Scattering reactions are matched at the second beam counter (BC2), entrance window, the target vessel, styrofoam cover. A selection in z < |13 cm| is applied to reject such reactions. The xy position at the reaction vertex is shown in (**c**), measured with the MWPCs in front of the target. The dashed line indicates the target cross section. Scattering at the target vessel at around (x = 2 cm, y = 2 cm) can be seen which is removed by the selection as indicated by the red circle.
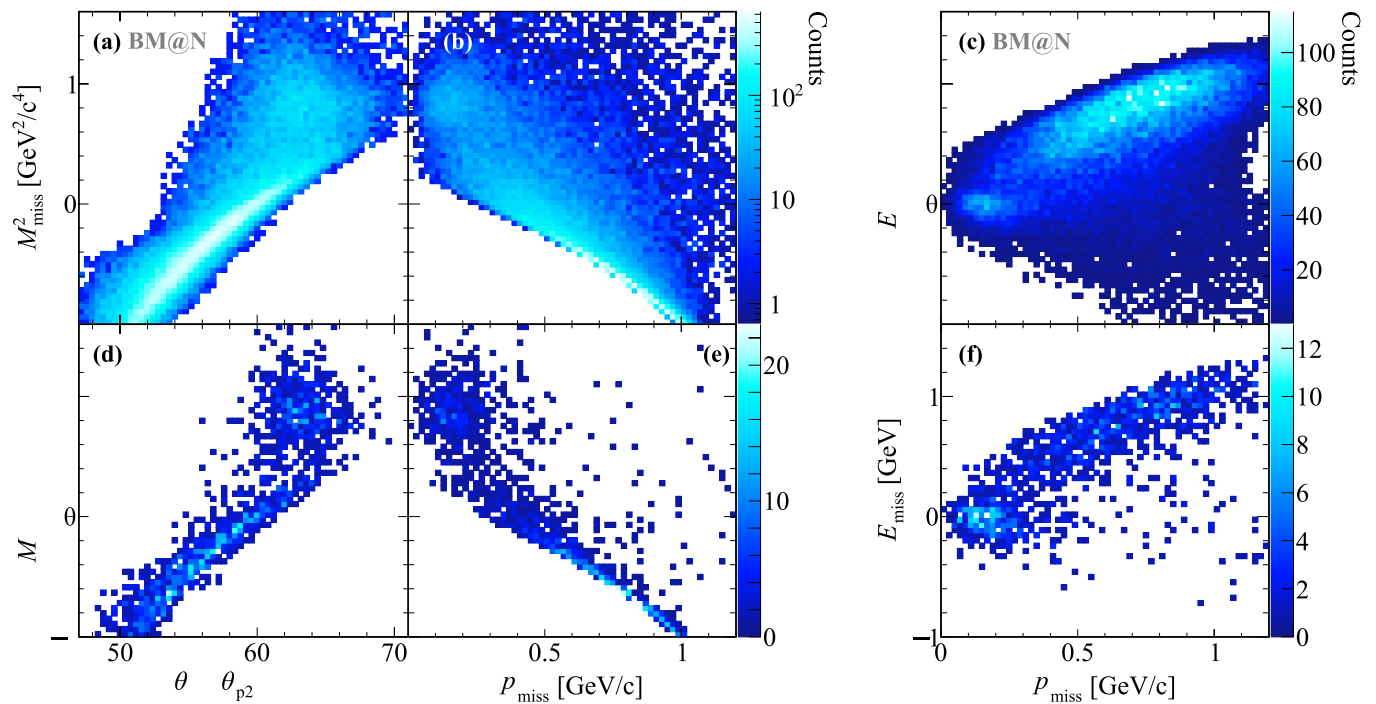
**Extended Data Fig. 3 | Kinematical correlations in single-proton knockout.** Figures (**a**)–(**c**) show the inclusive ^{12}C(p,2p) channel, and (**d**)–(**f**) the exclusive channel, that is with tagging ^{11}B. In both cases, the quasielastic peak (QE) and inelastic (IE) events are visible, while ISI/FSI are reduced by the fragment tagging. Eventually, a selection in E_{miss} and in-plane opening angle was chosen to select QE events, see Fig. 2. The distributions are not corrected for fragment-identification efficiency.
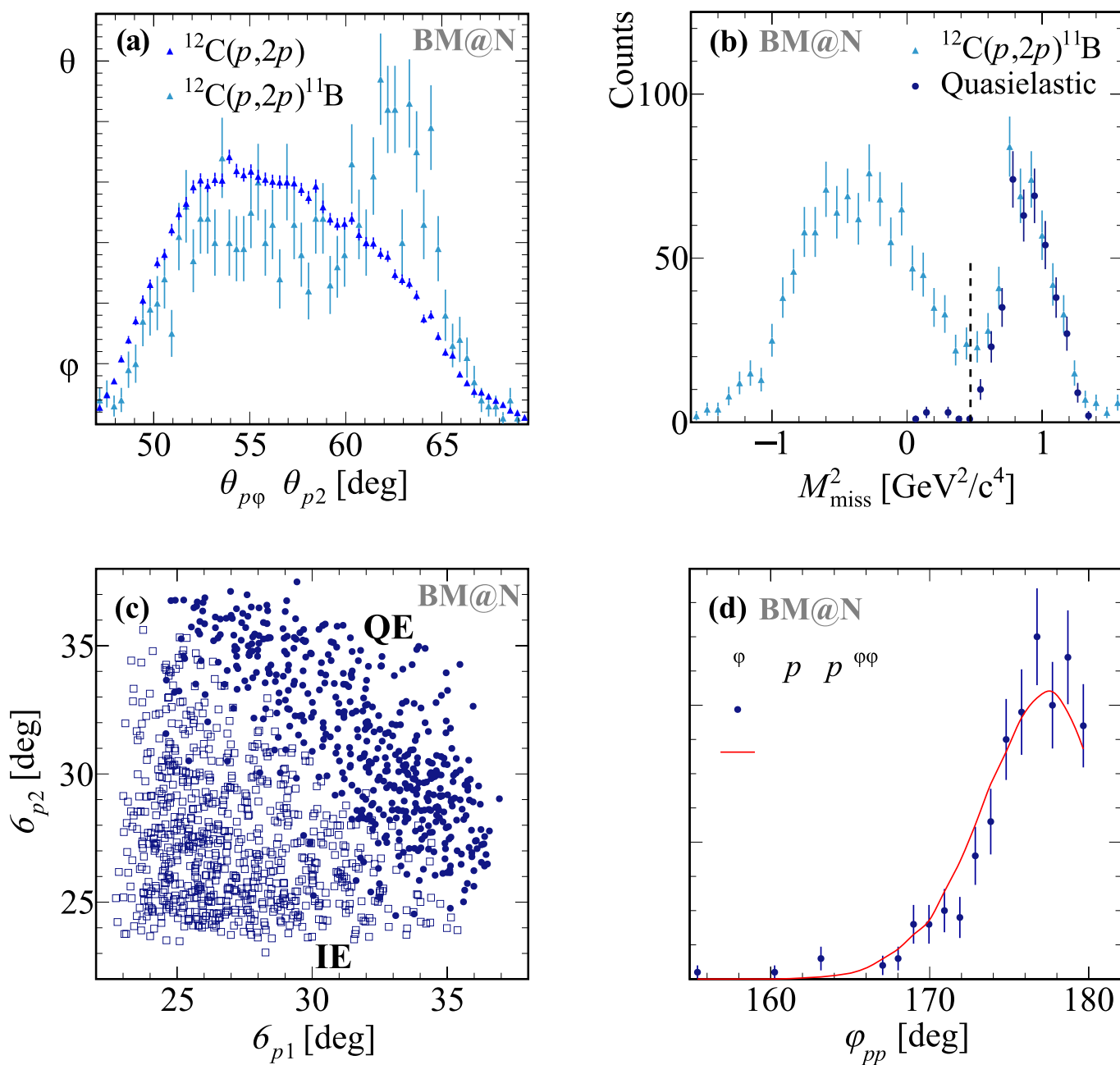
Extended Data Fig. 4 | Single-proton knockout signatures. a, Projection for in-plane opening angle ($\theta_{p1} + \theta_{p2}$) of Fig. 2, comparing the inclusive reaction ^{12}C(p,2p) and tagged events with ^{11}B coincidence. The inclusive distribution is area normalized to the tagged one. The fragment selection clearly suppresses FSI, and the QE signal separates from IE. **b**, Proton missing mass (M_{miss}^2) for tagged ^{12}C(p,2p)^{11}B events. After the QE selection in E_{miss} and in-plane opening angle, the distribution is shown in dark blue dots with artificial offset of 24 MeV/c in the positive x-axis direction for better visibility. We apply an additional missing mass cut $M_{miss}^2 > 0.47$ GeV^2/c^4, indicated by the dashed line. **c**, Angular correlation between the two (p,2p) protons for quasielastic ($M^2 > 0.55$ GeV^2/c^4, filled circles) and inelastic ($M_{miss}^2 < 0.55$ GeV^2/c^4, open squares) reactions only selected by missing mass. The QE events show a strong correlation with a polar opening angle of ~63°. **d**, The off-plane opening angle ψ_{pp} peaks at 180° as expected, shown for $M^2 > 0.55$ GeV^2/c^4. The width of this distribution is narrower than that dictated by the TAS acceptance. Data error bars show the statistical uncertainties of the data at the 1σ confidence level.
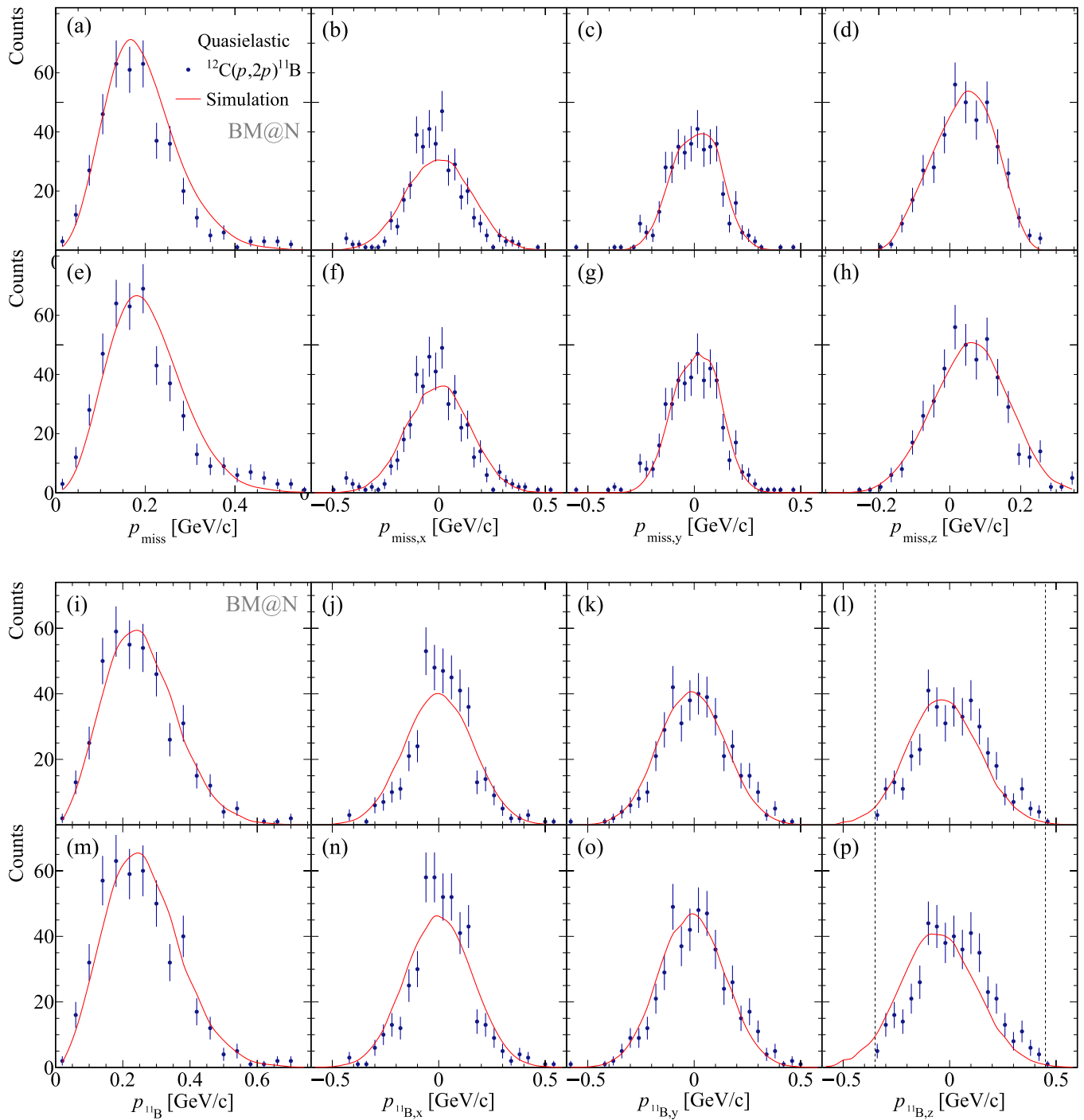
Extended Data Fig. 5 | Missing and fragment momentum. Momentum components for quasielastic ^{12}C(p,2p)^{11}B reactions compared to simulation. The proton missing momentum is shown for (**a**)–(**d**), while (**e**)–(**h**) show the same distributions but with missing mass cut only (0.55 GeV^2/c^4 < M$_{miss}^2$ <1.40 GeV^2/c^4). Agreement with the simulation is found in both cases. The shift in p$_{miss,z}$ is associated with a strong pp cross-section scaling with c.m. energy. For the same conditions the ^{11}B fragment momentum components are shown in (**i**)–(**l**), and (**m**)–(**p**). The dashed lines in p$_{^{11}B,z}$ indicate the momentum acceptance due to the fragment selection in P/Z. Data error bars show the statistical uncertainties of the data at the 1σ confidence level.
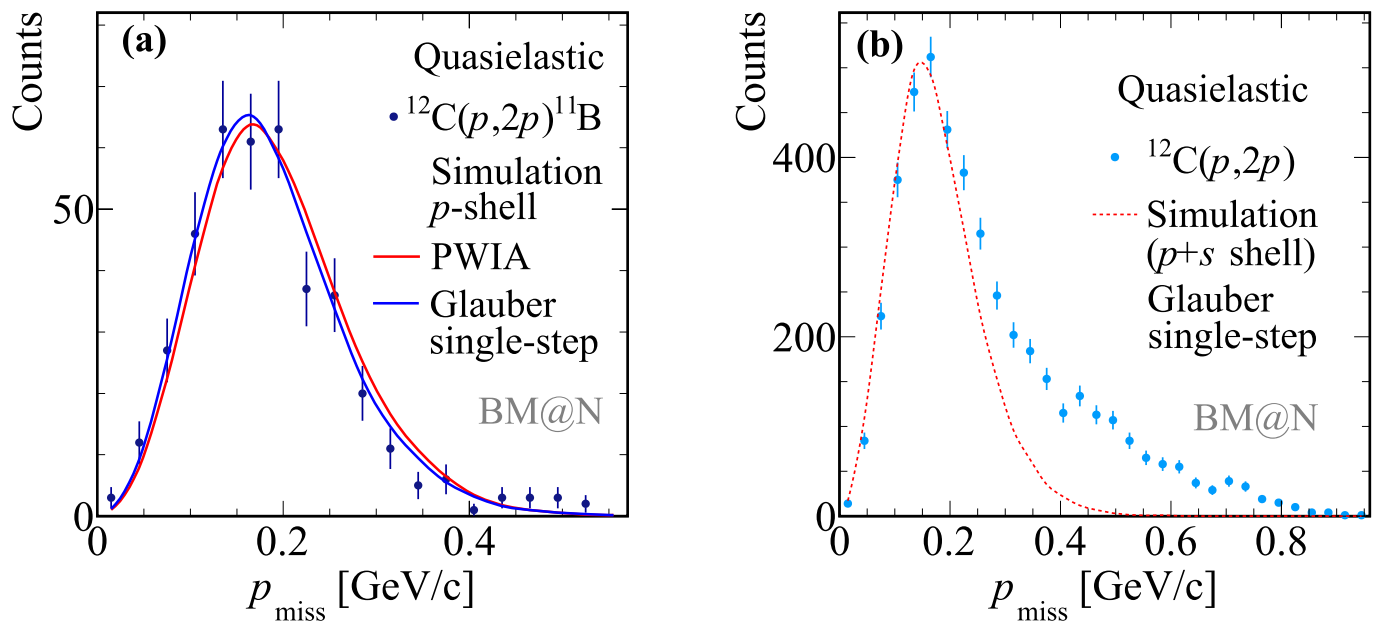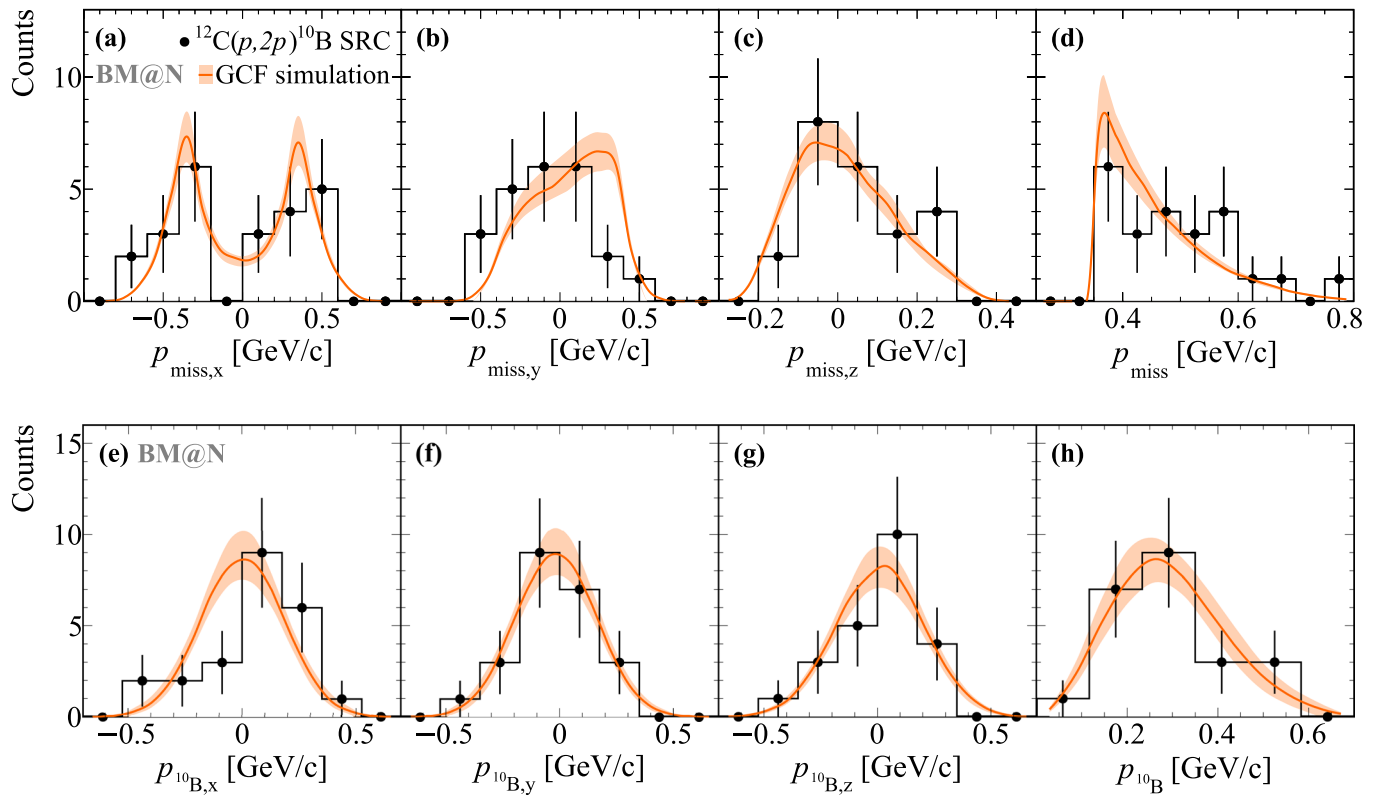
Extended Data Fig. 6 | Mean-field missing momentum calculations. a, Missing-momentum (p_{miss}) distribution for quasielastic ^{12}C(p,2p)^{11}B events, as in Fig. 3 of the main text. The data are compared with p-shell proton knockout simulation based on pwia (red line) and single-step scattering Glauber approximation calculation (blue line). Both calculations are normalized to the integral of the data. **b**, same as (**a**) only for inclusive quasielastic ^{12}C(p,2p) events. The data are compared with a single-step scattering Glauber approximation calculation including scattering off both p- and s-shell protons. The calculation is normalized to the data at low missing-momentum (below 250 MeV/c). Data error bars show the statistical uncertainties of the data at the 1σ confidence level.
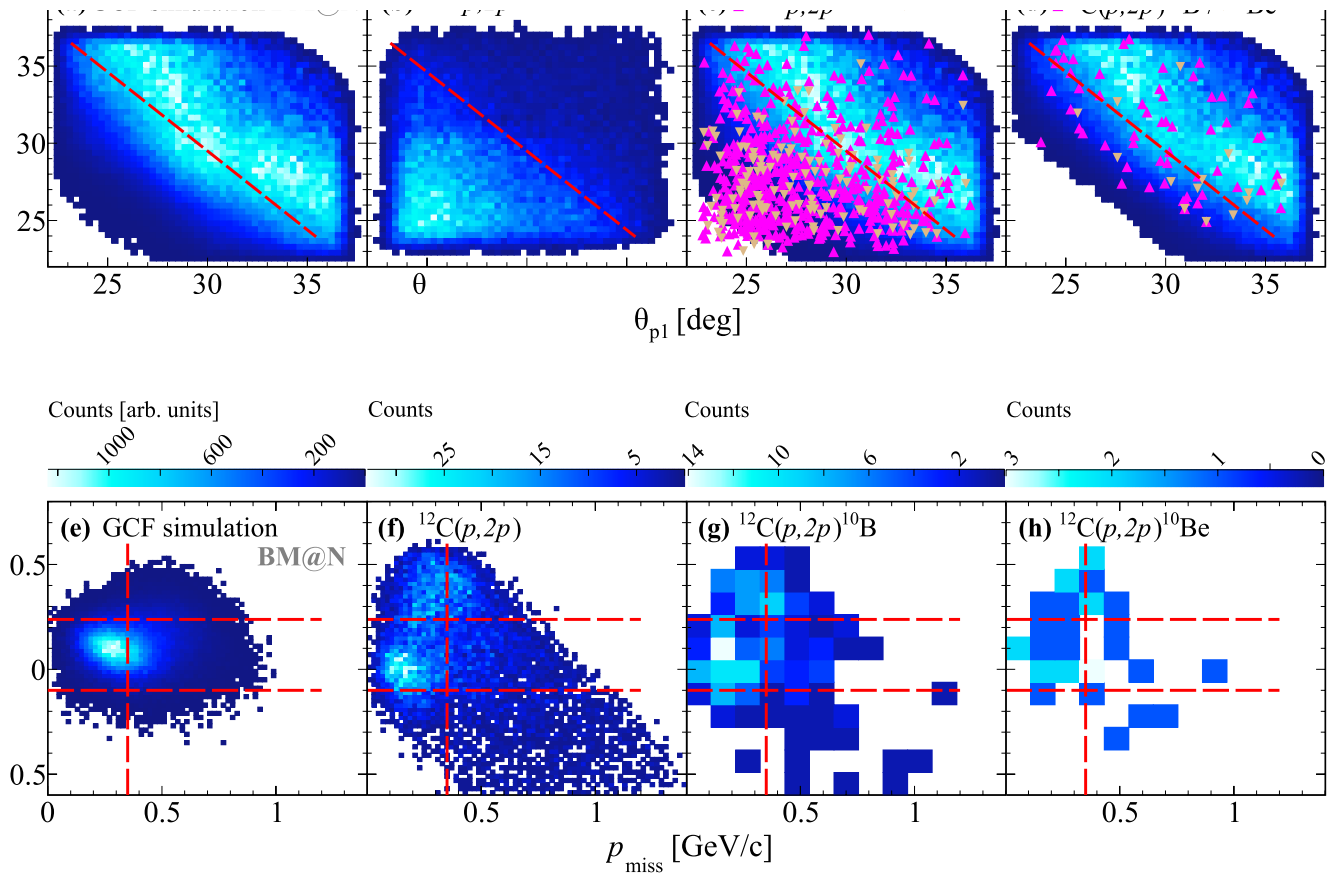
Extended Data Fig. 7 | SRC selection. The proton–proton polar angular correlations (θ_{p1} vs. θ_{p2}) are shown in (**a**)–(**d**) with $p_{miss} > 350$ MeV/c, the in-plane opening angle cut to be applied is indicated by the dashed line: (**a**) GCF simulation, (**b**) ^{12}C(p,2p) data, (**c**) ^{12}C(p,2p)^{10}B/Be data on top of simulation, and (**d**) the same as (**c**) but with additional E_{miss} cut. The missing energy (E_{miss}) vs. missing momentum (p_{miss}) is shown in (**e**)–(**h**): for (**e**) GCF simulation, (**f**) ^{12}C(p,2p), (**g**) ^{12}C(p,2p)^{10}B, and (**h**) ^{12}C(p,2p)^{10}Be events that pass the in-plane opening angle cut. The selection cuts in -110 MeV < E_{miss} < 240 MeV and $p_{miss} > 350$ MeV/c are indicated by the dashed lines.
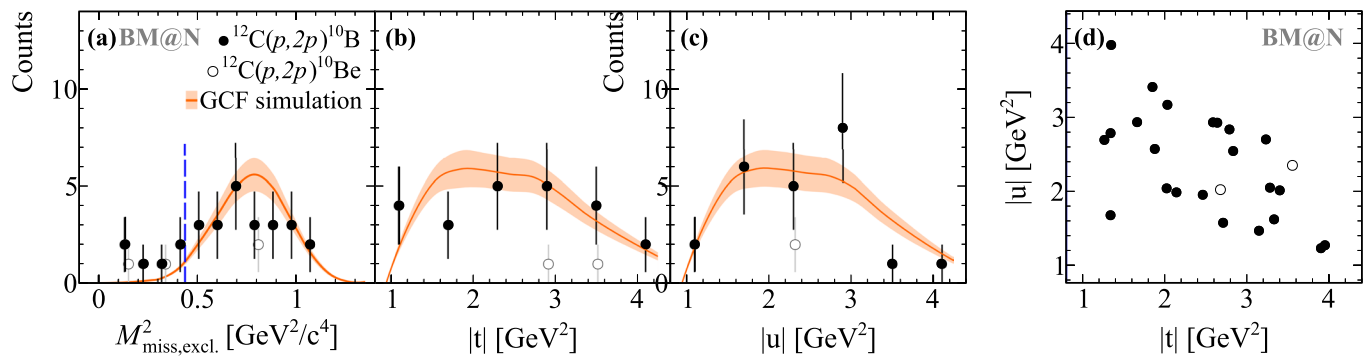
Extended Data Fig. 8 | SRC missing mass and momentum transfer. a, The exclusive missing mass ($M_{miss,excl.}^2$) distributions for $^{12}C(p,2p)^{10}B$ and $^{12}C(p,2p)^{10}Be$ events that pass the missing momentum, in-plane opening angle, and missing energy cuts together with the GCF simulation (orange). The vertical dashed blue line represents the applied cut on the exclusive missing-mass $M_{miss,excl.}^2 > 0.42$ GeV^2/c^4. **b**, and (**c**) represent the Mandelstam variables for the same cases, ^{10}B and ^{10}Be, (**d**) shows the two-dimensional momentum-transfer plot for ^{10}B. The width of the bands and the data error bars show the systematic uncertainties of the model and the statistical uncertainties of the data, respectively, each at the 1σ confidence level.

Extended Data Fig. 9 | SRC missing and fragment momentum. The missing momentum distributions (**a**)–(**d**) for the selected ^{12}C(p,2p)^{10}B SRC events (black) together with the GCF simulation (orange). Acceptance effects, especially in the transverse direction are well captured by the simulation. The lower figures (**e**)–(**h**) show the fragment momentum distributions in the rest frame of the nucleus for the same selected ^{12}C(p,2p)^{10}B SRC events (black) together with the GCF simulation (orange). The width of the bands and the data error bars show the systematic uncertainties of the model and the statistical uncertainties of the data, respectively, each at the 1σ confidence level.
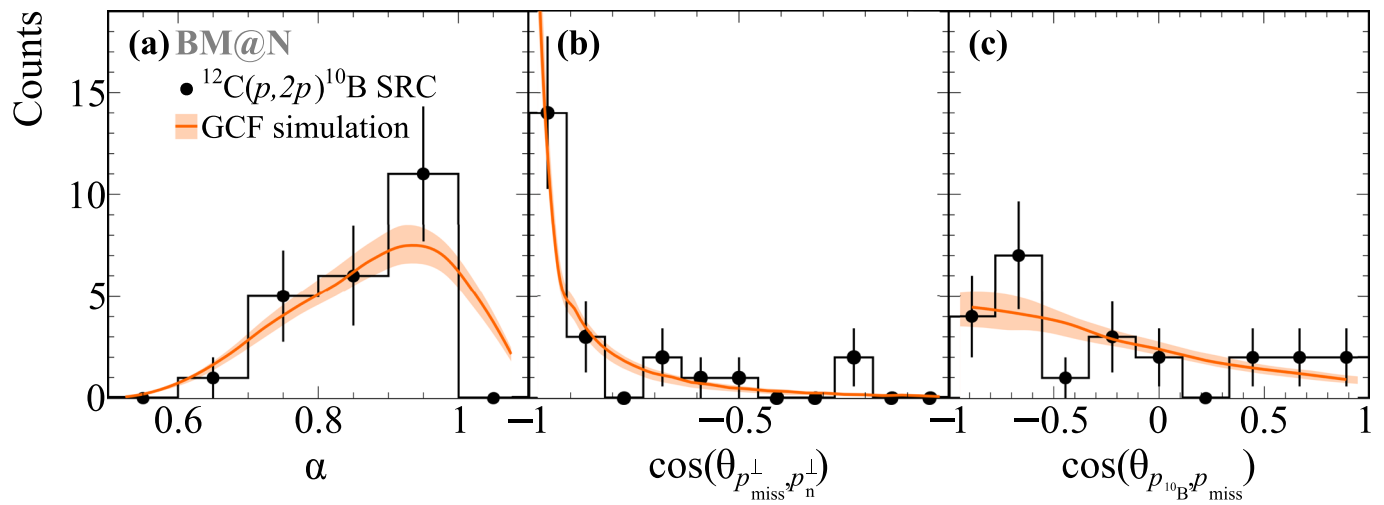
Extended Data Fig. 10 | SRC quantities. Selected $^{12}C(p,2p)^{10}B$ SRC events (black) together with the GCF simulation (orange). **a**, Light-cone momentum distribution $\alpha = (E_{miss} - p^z_{miss}/m_p)$. **b**, Cosine of the opening angle between the missing momentum and the neutron reconstructed momentum in the transverse direction, $\cos(\theta_{p^\perp_{miss},p^\perp_n})$. **c**, Cosine of the angle between the ^{10}B fragment and missing-momentum, $\cos(\theta_{p_{10B},p_{miss}})$. The width of the bands and the data error bars show the systematic uncertainties of the model and the statistical uncertainties of the data, respectively, each at the 1σ confidence level.